Supporting Information for

Quantitatively Assessing the Contributions of Dust Aerosols to Direct Radiative Forcing Based on Remote Sensing and Numerical Simulation

Determination of Radiation Fluxes

The direct radiative forcing (DRF) of aerosols is defined as the change in radiative flux due to its scattering and absorption by aerosols [S1,S2]. In this study, dust DRF at the surface (SFC) and the top of the atmosphere (TOA) was calculated by the difference between the net fluxes (downward minus upward) with and without dust with the following formulas [35]:

$$DRF_{TOA} = \Delta F_{TOA}(Dust) - \Delta F_{TOA}(noDust) \quad (1)$$

$$DRF_{SFC} = \Delta F_{SFC}(Dust) - \Delta F_{SFC}(noDust) \quad (2)$$

where DRF_{TOA} and DRF_{SFC} denote dust DRF at the TOA and the SFC under clear-sky conditions, respectively; ΔF is the net radiative flux at the specified layer; "Dust" denotes the case where the dust aerosol was included, and "noDust" denotes the case without dust aerosol.

In addition, dust DRF in the atmosphere (ATM) is defined as the divergence between DRF at TOA and at the SFC:

$$DRF_{ATM} = DRF_{TOA} - DRF_{SFC} \quad (3)$$

where DRF_{ATM} denotes dust DRF in the ATM.

Total surface fluxes provided by the model over northwest China were also calculated. The surface energy balance mainly consists of four main terms: net radiation, sensible heat flux, latent heat flux, and ground heat flux, determined by the surface energy budget (Q) equation [S3,S4]:

$$Q = LW^{\downarrow} - LW^{\uparrow} + (1 - A) * SW^{\downarrow} - (SH + LH + GH) \quad (4)$$

Where LW and SW are longwave and shortwave radiation fluxes, respectively; $\uparrow$ $\downarrow$ indicates the direction of the radiation fluxes upwards and downwards, respectively; A denotes surface albedo, which is a fraction of the incoming solar radiation reflected upward from the Earth's surface; GH denotes ground heat flux, which is the energy loss through the lower boundary by heat conduction [S3,S5]; and SH denotes sensible heat flux and LH denotes latent heat flux and both are positive upward, representing the energy loss from the Earth's surface to the atmosphere related to heat transfer and evaporation, respectively [S4]. All these radiant fluxes are in W/m^2 and are all positive.

Model Evaluation

At about 18:00 on 9 April, PM_{10} concentration increased sharply in Wuwei and Zhangye, indicating the start of dust events at both sites (Figure S1). The dust event in Wuwei ended at about 18:00 on 10 April and in Zhangye at about 10:00. The model underestimated the peak concentrations of PM_{10} at both sites, and the simulated peak time of PM_{10} had a lag. Although there were some differences between the simulated and the observed results, in general, variation trends of PM_{10} concentration were simulated. After dust emission concentration expanded by twice as much and was reduced by half, the PM_{10} concentration was then expanded and reduced by corresponding factors.

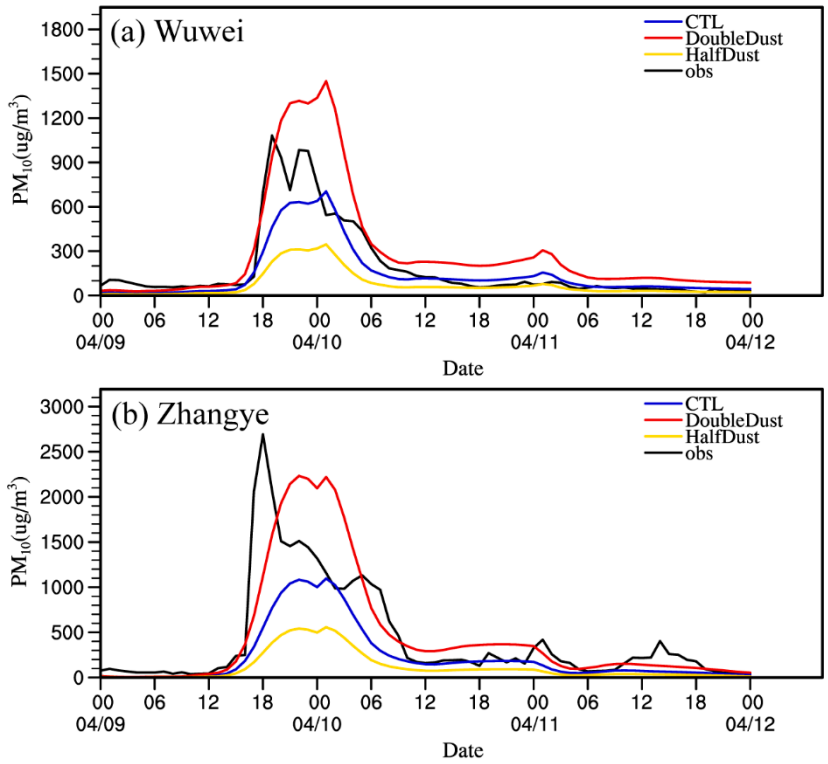

Figure S1. Time series of observed and modeled PM_{10} concentrations ($\mu g/m^3$) at the Wuwei and Zhangye sites during 9–12 April 2020: (**a**) Wuwei site, (**b**) Zhangye site. The locations of the two sites are indicated in Figure 1 in red.

The pattern of surface temperature in Western China was high in the northwest and low in the southwest, and high temperatures were mainly located in southern Xinjiang (up to 20.1 ℃) and low temperatures mainly in the Himalayas and Kunlun Mountains (low to –15.7 ℃). In general, the simulated surface temperature was almost consistent with the surface temperature obtained from FNL reanalysis data, especially in the Taklimakan Desert (Figure S2). Within the study area, the FNL and simulated average surface temperature was 6.50 and 6.08 ℃, respectively. Similar to the results of Chen et al. [30,S6], the underestimation of the model occured mainly in the Tibetan Plateau, which was beyond the scope of the dust event occurring in this study.

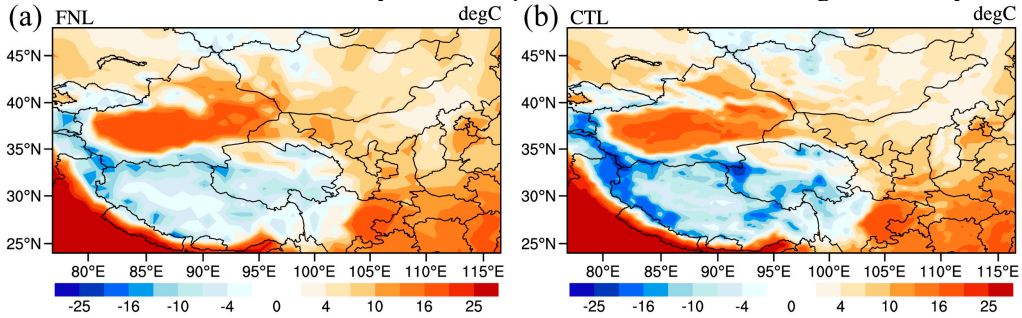

Figure S2. The NCEP/FNL reanalysis data and simulated average temperature at 2 m and from 9–12 April 2020: (**a**) FNL, (**b**) CTL.

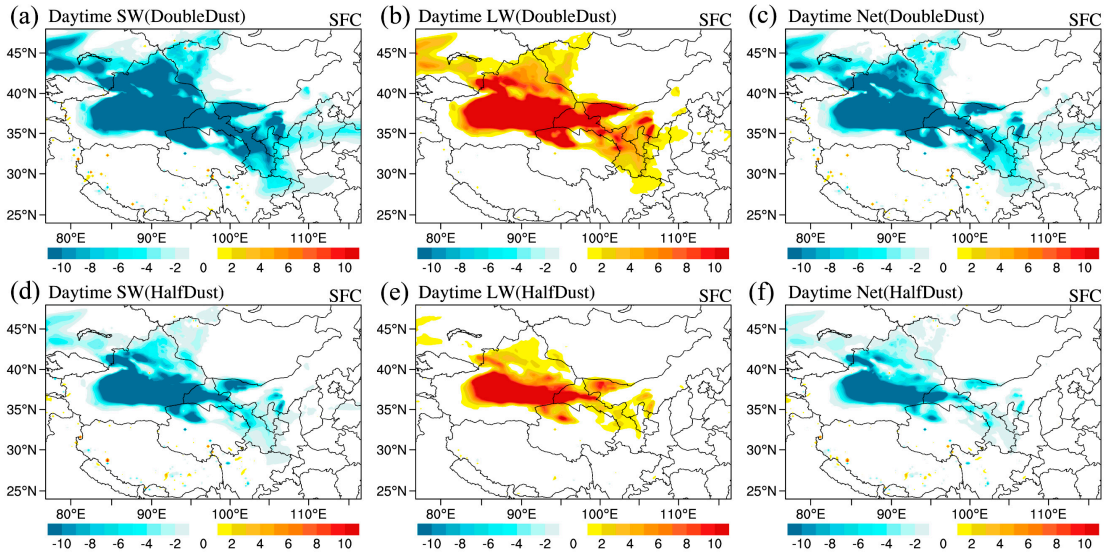

Figure S3. Spatial distribution of daytime dust DRF (W/m^2) at SFC under clear-sky conditions from DoubleDust and HalfDust simulation averaged during 9–12 April 2020: (**a**) SW from DoubleDust, (**b**) LW from DoubleDust, (**c**) net from DoubleDust, (**d**) SW from HalfDust, (**e**) LW from HalfDust, (**f**) net from HalfDust.

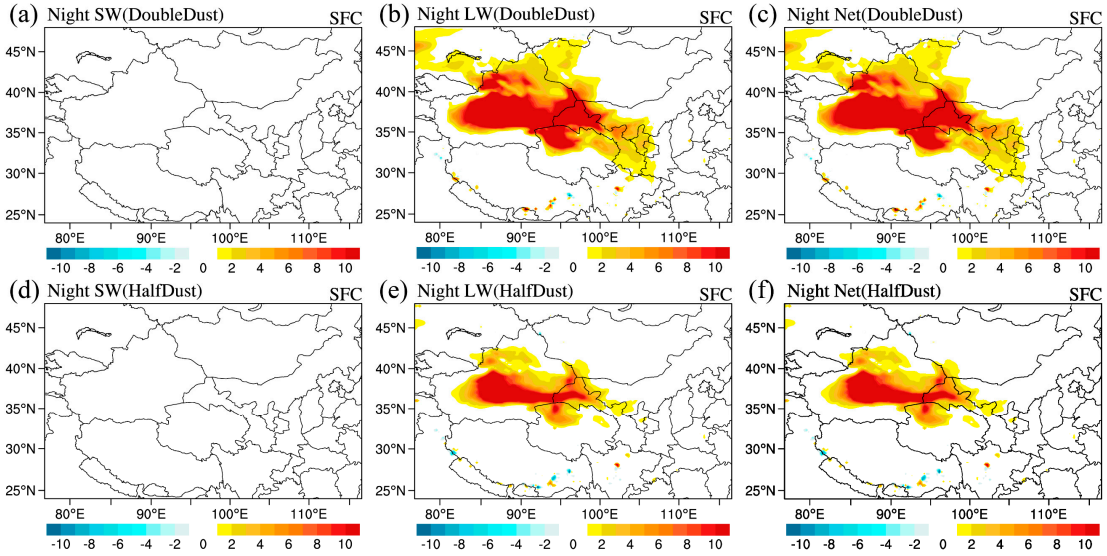

Figure S4. Spatial distribution of nighttime dust DRF (W/m^2) at SFC under clear-sky conditions from DoubleDust and HalfDust simulation averaged during 9–12 April 2020: (**a**) SW from DoubleDust, (**b**) LW from DoubleDust, (**c**) net from DoubleDust, (**d**) SW from HalfDust, (**e**) LW from HalfDust, (**f**) net from HalfDust.

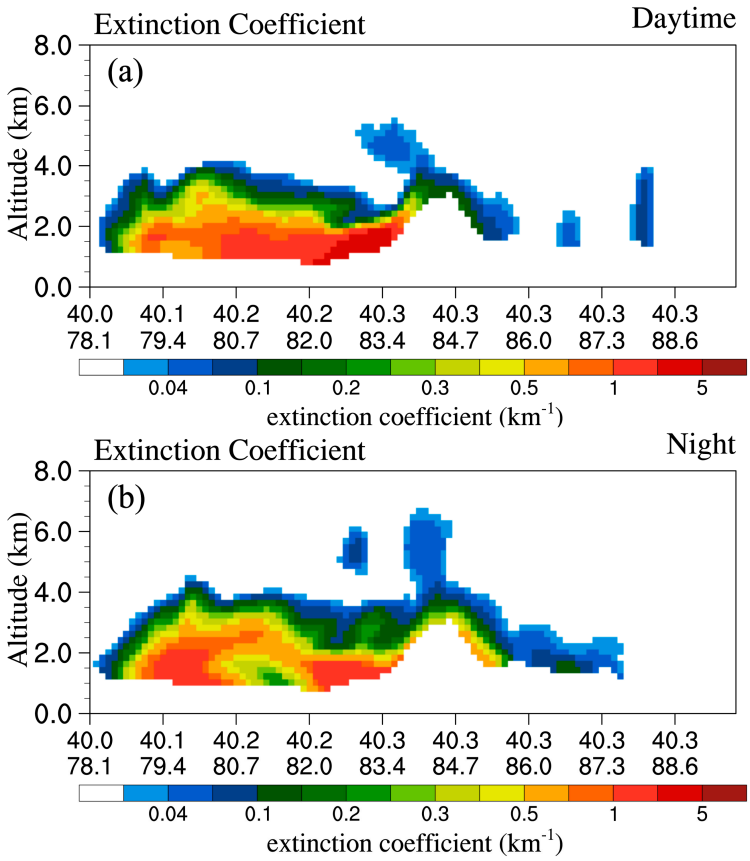

Figure S5. Cross-sections of the simulated daytime and nighttime extinction coefficients (km^{-1}) at 532 nm along the dust transport path from CTL averaged during 9–12 April 2020: (**a**) averaged extinction coefficient during the day, (**b**) averaged extinction coefficient at night.

Table S1. Summary of geographical locations and ground-based sites for this study.

Location	Latitude	Longitude	Altitude	Period
Dust source region (DSR)	37° N–45° N	77° E–100° E	–	–
Dust affected region (DAR)	33° N–42° N	100° E–108° E	–	–
Wuwei	37°55'57" N	102°38'55" E	1527 m	2020.4.9-2020.4.12
Zhangye	38°56'48" N	100°28'7" E	1473 m	2020.4.9-2020.4.12

Table S2. Summary of the description of the satellite data for this study. The orbital path of CALIPSO is in Figure 1.

Data Set	Parameter	Latitude	Longitude	Spatial Resolution	Temporal Resolution	Period/Time	Number of Data	Number of Data from Each Satellite
MODIS	AOD (550 nm)	27° N–52° N	72° E–118° E	10×10 km	5 minutes	06:00 11 April 2020	4	2(Terra), 2(Aqua)
CALIPSO	Extinction coefficient (532 nm)	—	—	60 m (vertically), 5 km (horizontally)	5.92 seconds	07:00 11 April 2020	1	1 (CALIPSO)
CERES	Radiation fluxes (TOA, SFC)	24° N–50° N	77° E–125° E	1°×1°	1 hour	9 April 2020–12 April 2020	36	72 (Terra + Aqua)

Support Information References

1. Sokolik, I. N.; Winker, D. M.; Bergametti, G.; Gillette, D. A.; Carmichael, G., Kaufman, Y. J.; et al. Introduction to special section: Outstanding problems in quantifying the radiative impacts of mineral dust. J. Geophys. Res.-Atmos. **2001**, 106(D16): 18015-18027. doi:10.1029/2000jd900498
2. Heald, C. L.; Ridley, D. A.; Kroll, J. H.; Barrett, S. R. H.; Cady-Pereira, K. E.; Alvarado, M. J.; et al. Contrasting the direct radiative effect and direct radiative forcing of aerosols. Atmos. Chem. Phys. **2014**, 14(11): 5513-5527. doi:10.5194/acp-14-5513-2014
3. Kantha, L. H. and Clayson, C. A. Chapter 4 surface exchange processes. International Geophysics **2000**, 67, 417–509. doi: 10.1016/S0074-6142(00)80080-7
4. Parker, D. J. et al. Local weather. In Meteorology of Tropical West Africa, ed. Parker, D. J. and Diop-Kane, M. (Wiley, Hoboken) **2017**, 130–174.
5. Hartmann, D. L. Chapter 4 the energy balance of the surface. International Geophysics **1994**, 56, 81-114.

6. Chen, S. Y.; Yuan, T. G.; Zhang, X. R.; Zhang, G. L.; Feng, T. C.; Zhao, D.; et al. Dust modeling over East Asia during the summer of 2010 using the WRF-Chem model. J. Quant. Spectrosc. Radiat. Transf. **2018**, 213: 1-12. doi:10.1016/j.jqsrt.2018.04.013